

Gate modulation of the hole singlet-triplet qubit frequency in germanium

John Rooney, Zhentao Luo, and Hong-Wen Jiang
Physics and Astronomy Department, University of California, Los Angeles

Lucas E. A. Stehouwer, Giordano Scappucci, and Menno Veldhorst
QuTech and Kavli Institute of Nanoscience, Delft University of Technology
(Dated: November 20, 2023)

Spin qubits in germanium gate-defined quantum dots have made considerable progress within the last few years, partially due to their strong spin-orbit coupling and site-dependent g -tensors. While this characteristic of the g -factors removes the need for micromagnets and allows for the possibility of all-electric qubit control, relying on these g -tensors necessitates the need to understand their sensitivity to the confinement potential that defines the quantum dots. Here, we demonstrate a $S - T_-$ qubit whose frequency is a strong function of the voltage applied to the barrier gate shared by the quantum dots. We find a g -factor that can be approximately increased by an order of magnitude adjusting the barrier gate voltage only by 12 mV. We attribute the strong dependence to a variable strain profile in our device. This work not only reinforces previous findings that site-dependent g -tensors in germanium can be utilized for qubit manipulation, but reveals the sensitivity and tunability these g -tensors have to the electrostatic confinement of the quantum dot.

I. BACKGROUND AND OBJECTIVES

Utilizing hole spin states in strained germanium (Ge/SiGe) gate-defined quantum dots for qubit operation has developed rapidly over the past several years, as groups have demonstrated fast two-qubit logic [1], singlet-triplet encodings [2], and a four-qubit quantum processor [3]. The success of these experiments can partly be attributed to the various advantages of holes for spin qubit encoding [4]. In stark contrast to electrons, the two topmost valence bands in Ge are well separated in energy due to strain and 2D confinement. The light effective mass ($0.054m_e$ [5]) of holes in the topmost band and the absence of valley degeneracy allows us to easily access the two highest hole states for spin encoding. Furthermore, Ge hole spin coherence times benefit from their weak hyperfine interaction with surrounding nuclear spins. Finally, because of their strong spin-orbit coupling and site-dependent g -tensors, Ge hole quantum dots do not require the fabrication of micromagnets, advancing their potential for scalability and integration into current industrial semiconductor facilities [4].

Most double quantum dot singlet-triplet qubit studies have focused on encodings between the singlet $|S\rangle$ and unpolarized triplet $|T_0\rangle$ states [2, 6–8]. In this work, we detail the dynamics of the $S - T_-$ subspace, which has been less studied thus far [9–11]. Furthermore, we explore the tunability of the hole g -tensors by varying the electrostatic potential generated by the barrier gate bridging the two quantum dots. As quantum computation with Ge hole spins critically depends on the g -tensor, the ability to manipulate the g -tensor becomes a valuable asset for a spin qubit encoded in this system.

II. RESULTS

A scanning electron microscope image of the device studied is shown in Fig. 1a along with the Ge/SiGe heterostructure in Fig. 1b. The strained Ge quantum well is 16 nm in width and located 55 nm below the surface. For more details regarding the heterostructure, see [5]. A two-dimensional hole gas is first created in the Ge well by applying a negative voltage to a global top gate situated above the heterostructure. The double quantum dot (DQD) is then formed underneath plungers P_1 and P_2 by applying appropriate voltages to the neighboring barrier gates, where the middle barrier voltage V_B controls the coupling between the two dots. Varying the plunger voltages controls the chemical potential of each dot, allowing us to reach the few-hole regime (Fig. 1c), where all experiments were performed at the (1,1)-(0,2) anticrossing (Fig. 1d). The hole occupation of both dots was detected by the nearby SET (left half of the device) labeled in Fig. 1a. For convenience in describing this DQD system, we define the relative energy of the two quantum dots as the detuning $\epsilon = \alpha_2 V_{P_2} - \alpha_1 V_{P_1}$, where α_i converts the voltage applied to P_i to the change in the energy level of dot i . Fig. 1d illustrates the detuning axis on the stability diagram, where $\epsilon = 0$ at the (1,1)-(0,2) boundary.

When the system passes the $\epsilon = 0$ detuning line into the (1,1) charge configuration, the (0,2) singlet state hybridizes with the (1,1) singlet due to the tunnel coupling between the quantum dots: $|S\rangle = \sin(\Omega/2)|S_{02}\rangle - \cos(\Omega/2)|S_{11}\rangle$. Here, $\Omega = \arctan\left(\frac{2\sqrt{2}t_\epsilon}{\epsilon}\right)$ is the mixing angle between the two singlet states. In addition to $|S\rangle$, Fig. 2c depicts the three triplet states that compose the four lowest energy levels in the (1,1) charge configuration. A simple block magnet situated near the device's PCB provided the field necessary to lift the degeneracy of the

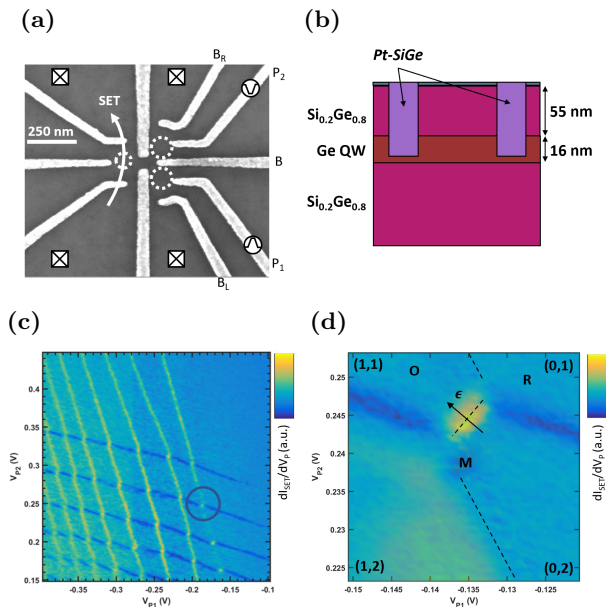


FIG. 1: **(a)** SEM image of lithographically defined gates identical to the device used in this study. **(b)** Heterostructure of the device showing the Ge quantum well packed between two Ge rich SiGe layers. **(c)** A typical stability diagram with the circle highlighting the (1,1)-(0,2) anticrossing. **(d)** All experiments were completed at the (1,1)-(0,2) anticrossing, where (n,m) denotes the hole occupation for each dot. Point R was used to reset the DQD, M for measurement and initialization, and O for coherent operation between the singlet and triplet states.

three triplet states, generating an estimated fixed global out-of-plane field of 1.2 mT and in-plane field of 4.4 mT measured at the device's position ($|\mathbf{B}| = B = 4.6$ mT points $\theta = 15^\circ$ out of the x-y plane). This tilted field differs from previous qubit experiments on this heterostructure where B was completely in-plane, allowing for a unique perspective into the hole spin states [3, 11]. Importantly, this magnetic field splits the polarized triplet $|T_-\rangle$ from $|T_0\rangle$ by the average Zeeman energy of the quantum dots \bar{E}_z .

Beginning at M in Fig. 1d, the system is first initialized into the (0,2) singlet state. A voltage pulse was then applied to P_1 and P_2 to quickly separate the holes and create a small admixture between the (1,1) singlet $|S\rangle = \frac{1}{\sqrt{2}}(|\uparrow\downarrow\rangle - |\downarrow\uparrow\rangle)$ and polarized triplet $|T_-\rangle = |\downarrow\downarrow\rangle$ states. Once the holes were separated, the system was pulsed to various operation detunings ϵ_P and allowed to evolve for a time t_E between $|S\rangle$ and $|T_-\rangle$ (Fig. 2a and 2c). The qubit frequency (Fig. 2b) is given by the energy difference between these two states at the operation detuning: $hf = \Delta E_{ST_-}$, which plateaus to roughly \bar{E}_z for large detunings.

For smaller operation detunings, the energy splitting reaches a minimum at the $S - T_-$ anticrossing, where it

approximately equals $2\Delta_{ST_-}$. We define Δ_{ST_-} as the coupling between $|S\rangle$ and $|T_-\rangle$ at the $S - T_-$ anticrossing. By varying the operation detuning ϵ_P from 0.5 to 2.5 meV, we sampled the energy splitting between the two lowest states for both regimes. The existence of this minimum leads to the observed chevron pattern at 1 meV in Fig. 2a, which has been seen in previous $S - T_-$ works and absent from studies coherently manipulating the $S - T_0$ states [2, 6–11].

To understand these dynamics, we utilize a Hamiltonian describing the $\{|S\rangle, |T_-\rangle\}$ subspace that was derived in Ref. [12] and is a reduced form of the full model used in Ref. [9]. To leading order, it takes the following form:

$$H = \begin{pmatrix} -J(\epsilon) & \Delta \\ \Delta & -\bar{E}_z \end{pmatrix}. \quad (1)$$

We define the exchange energy $J(\epsilon) = -\frac{\epsilon}{2} + \sqrt{\frac{\epsilon^2}{4} + 2t_c^2}$ as the energy difference between $|S\rangle$ and $|T_0\rangle$. The coupling of the $S - T_-$ states (Δ) emerges from two sources: (1) a spin-orbit splitting (Δ_{so}) and (2) an effective Zeeman splitting due to the anisotropy of the g -tensors (g_a) that is only present when B has non-zero in- and out-of-plane components: $\Delta = |\Delta_{so} \sin(\frac{\theta}{2}) + g_a \mu_B B \cos(\frac{\theta}{2})|$ [9, 12]. The anisotropy between the in- and out-of-plane g -factors of a quantum dot has been previously observed, where the in-plane g -factors (g_{\parallel}) were measured to be a few tens to hundreds of times smaller than their out-of-plane counterparts (g_{\perp}) for holes in Ge/SiGe substrates [9, 13]. The $|T_-\rangle$ state splits from $|T_0\rangle$ by the average Zeeman energy, $\bar{E}_z = \bar{g} \mu_B B$, where \bar{g} is the average g -factor of the two dots projected onto the axis of \mathbf{B} .

With this Hamiltonian, we can solve for the frequency of the $S - T_-$ evolution: $f = \frac{1}{h} \sqrt{(J - \bar{E}_z)^2 + (2\Delta)^2}$. At the $S - T_-$ anticrossing, $J = \bar{E}_z$, and f is controlled by Δ , where X rotations are performed around the Bloch sphere (Fig. 2d). For large detunings, $J \rightarrow 0$, leaving f to be determined by the average Zeeman energy and $S - T_-$ coupling, and the qubit rotates near the z axis. The larger the ratio $\frac{\bar{E}_z}{\Delta}$ becomes, the closer this axis aligns with the z direction. We note that with control over the orientation of the magnetic field, it is possible for $\Delta \rightarrow 0$ at specific detunings, resulting in perfect Z rotations [12].

After manipulation, the separated holes were reunited in the (0,2) charge configuration at M for spin readout of the final state using Pauli spin blockade. The system is then reset at R before repeating the cycle again. For a detailed explanation of each step of the pulse, see section SI of the supplementary material.

We first analyzed the dephasing and relaxation of this qubit by measuring T_2^* and T_1 . For each ϵ_P in Fig. 2a, the $S - T_-$ evolution was fit to a Gaussian damped sinusoid $P = Ae^{-(t/T_2^*)^2} \cos(\omega t + B) + Ce^{-t/D} + E$, where T_2^* is the inhomogeneous dephasing time. For example traces and details relating to this fit, see section SII. After extracting T_2^* as a function of ϵ_P (Fig. 3a), a clear dependence on the pulse height is seen. This behavior can

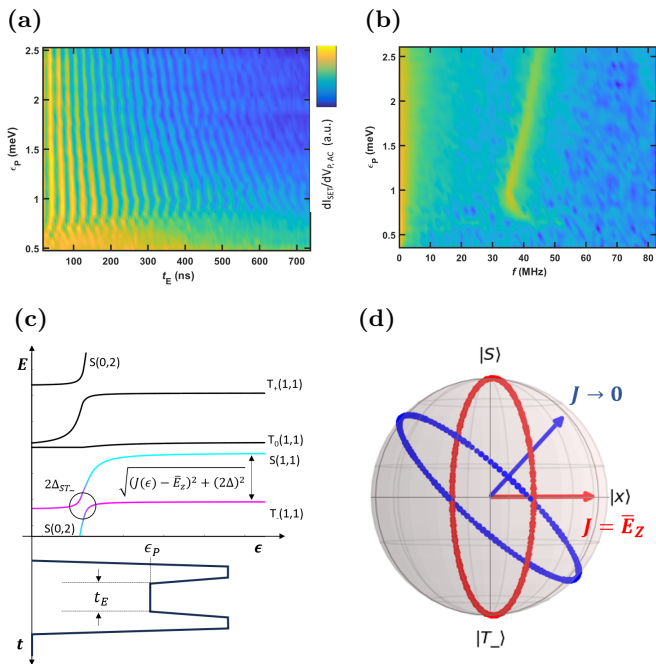


FIG. 2: (a) The SET signal as a function of the detuning and evolution time, illustrating coherent oscillations between $|S\rangle$ and $|T_-\rangle$. The chevron pattern located near 1 meV arises from the $S - T_-$ anticrossing defined by the energy splitting Δ_{ST_-} , while oscillations at large detunings are controlled by the average Zeeman energy of the two dots: \bar{E}_z . (b) Fourier transform of the coherent oscillations in (a), illustrating the $S - T_-$ energy splitting as a function of detuning. (c) Energy levels (not to scale) of the singlet and triplets as a function of detuning. The Ramsey pulse used is shown below as a function of time and detuning. (d) Bloch sphere depicting the two rotation axes for the $S - T_-$ subspace. When ϵ_P is at the $S - T_-$ anticrossing, the system undergoes X rotations (red axis). For large detunings, a combination of X and Z rotations are performed (blue).

be understood with a simple model describing the influence of charge and magnetic noise on the fluctuations in the energy difference between the two states [2, 6]:

$$\sqrt{2}\hbar T_2^{*-1} = \sqrt{\langle \delta E^2 \rangle}. \quad (2)$$

At the $S - T_-$ anticrossing where the qubit frequency reaches a minimum, the system is insensitive to first-order to fluctuations in ϵ due to charge noise. This protection leads to the maximum in T_2^* seen at 1 meV in Fig. 3a. However, the qubit is still susceptible to electrical noise affecting the dot g -factors and tunnel coupling as well as magnetic noise afflicting B . We can estimate the magnitude of this noise combination from Eqn. 2 using the fact that $J = \bar{E}_z$ at this detuning. Under this condition $\delta E = 2\delta\Delta_{\text{rms}}$, where we define $\delta\Delta_{\text{rms}}$ to include

the noise sources pertinent to t_c , g_a , and B , leading to

$$\delta\Delta_{\text{rms}} \approx \frac{\sqrt{2}\hbar}{2} (T_2^* = 600 \text{ ns})^{-1} = 0.8 \text{ neV}.$$

For large operation detunings, the energy separation between the $S - T_-$ states reaches a parallel regime (Fig. 2b), which diminishes the charge noise contribution to δE . In this regime, Δ_{ST_-} approximately equals \bar{E}_z , where the combined electrical and magnetic "Zeeman" noise affecting \bar{g} and B limits T_2^* . We estimate this parameter using Eqn. 2 again:

$$\begin{aligned} \delta E &\approx \delta\bar{E}_{z,\text{rms}}, \\ \delta\bar{E}_{z,\text{rms}} &\approx \sqrt{2}\hbar(T_2^* = 317 \text{ ns})^{-1} = 3 \text{ neV}. \end{aligned}$$

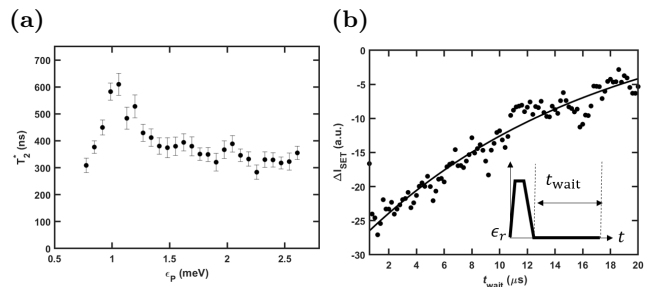


FIG. 3: Dephasing and relaxation measurements (a) T_2^* as a function of detuning. Linecuts in Fig. 2a are fit to the curve $P = Ae^{-(t/T_2^*)^2} \cos(\omega t + B) + Ce^{-t/D} + E$, where the dephasing time T_2^* is extracted and plotted in (a). Error bars equal one standard deviation of the uncertainty in T_2^* from this fit. This decoherence can be understood as a contribution from two noise terms with the simple model shown in Eqn. 2. From this model, we estimate $\delta\Delta_{\text{rms}} = 0.8$ and $\delta\bar{E}_{z,\text{rms}} = 3$ neV. (b) A T_1 measurement where the change in SET current is recorded as a function of wait time at the measurement point M. We extract T_1 from the fit $P = Ae^{-(t/T_1)} + B$ (solid line) and calculate $T_1 = 17.2 \pm 3.2 \mu\text{s}$. Inset: the pulse used to observe this decay.

The system's T_1 spin relaxation time was measured by varying the wait time at the readout position ϵ_r (Fig. 3b). For these measurements, the system was allowed to completely dephase at the operation detuning ϵ_P before being pulsed back to the readout window for a variable amount of time (see inset of Fig. 3b). We fit the resulting exponential decaying curve shown in Fig. 3b to $P = Ae^{-(t/T_1)} + B$ and find T_1 to be $17.2 \pm 3.2 \mu\text{s}$, which is comparable to experiments done in single hole [1] and $S - T_0$ qubits [2]. However, this T_1 can still be improved, as single hole spin relaxation times as long as 32 ms with $B = 0.67$ T have been measured using tighter dot confinements and limiting the dot-reservoir coupling [14].

We now focus on modulating the coherent evolution

of the $S - T_-$ states by adjusting the voltage applied to the barrier separating the two quantum dots. Over a small range of voltage (12 mV), Fig. 4 illustrates the dramatic transformation the $S - T_-$ oscillations undergo. As V_B increases, it is clear the frequency of evolution between the two states decreases monotonically. From the Fourier transform of these oscillations, we can isolate two quantities of interest, namely \bar{g} from the frequency at large detuning following $f \sim \bar{E}_z/h$ and Δ_{ST_-} from the minimum frequency near $\epsilon_P = 1$ meV, where $f = 2\Delta_{ST_-}/h$.

We would like to note that the location of the frequency minimum ϵ_* is determined by the tunnel coupling t_c and \bar{E}_z from the condition $J = \bar{E}_z$ [9]:

$$\epsilon_* = \frac{2t_c^2 - \bar{E}_z^2}{\bar{E}_z}, \quad (3)$$

Because ϵ_* remains approximately constant throughout this range of V_B , a decrease in t_c must be accompanied by a decrease in \bar{E}_z . While it is evident from the sharper rises seen in the FFTs of Fig. 4 that t_c decreases with V_B , a similar decline in \bar{E}_z , and therefore \bar{g} , is necessarily present. From the $S - T_-$ evolution frequency at large ϵ_P in Fig. 4, we can then extract the dependence of \bar{g} on V_B .

III. DISCUSSION

Fig. 5 demonstrates the linear trend both Δ_{ST_-} and \bar{g} follow with respect to the barrier voltage V_B . Recall the $S - T_-$ coupling is determined by both the spin-orbit coupling and the effect of the anisotropic g -tensors, g_a . We assert it is the latter of these contributions that is affected over the small range of V_B considered here. Consequently, to justify the modulation of the qubit frequency in Fig. 5, we seek a mechanism that simultaneously reduces both \bar{g} and g_a as V_B increases. We will argue these changes are accomplished through increasing the admixture of light-hole (LH) states into the predominantly heavy-hole (HH) ground state of the Ge quantum dot.

While it is well known the upper valence bands in Ge/SiGe heterostructures are composed primarily of HH states due to a large HH-LH splitting Δ_{HL} [4], an accurate understanding of the g -tensor in many Ge materials requires the consideration of the LH bands [15–17]. To understand the consequences of this mixing, it is beneficial to first examine the g -factor components of both bands in the case of bulk Ge. As described in Refs. [16, 18, 19], for the pure HH state, the out-of-plane g -factor is $g_\perp = 6\kappa + \frac{27q}{2}$ and the in-plane component is $g_\parallel = 3q$, where $\kappa = 3.41$ and $q = 0.07$ are the magnetic Luttinger parameters. Note this κ and q result in the large anisotropy of the g -tensor: $g_\perp \gg g_\parallel$. Conversely, for pure LH states, $g_\perp = 2\kappa$ and $g_\parallel = 4\kappa$. Compar-

ing these two bands, the LH state has a smaller g_\perp but greater g_\parallel compared to the HH state. Therefore, when increasing the LH admixture in the ground state of the quantum dot, we expect a decrease in g_\perp and an increase in g_\parallel , which has been experimentally observed for various mixing mechanisms [9, 16, 17, 19].

Due to the large anisotropy between g_\perp and g_\parallel , \bar{g} is dominated by its out-of-plane component \bar{g}_\perp . With an increase in HH-LH mixing, we then expect a decrease in \bar{g} through a reduction in g_\perp for either dot. On the other hand, the in-plane g -factors are the leading order terms defining g_a , where a more similar g_\parallel between the two dots diminishes g_a . Increasing the HH-LH mixing decreases g_a when the in-plane g -factors change in such a way that the difference between g_\parallel for the left and right dot lessens. Importantly, this mixing mechanism can then explain both downward trends we observe in Fig. 5.

Although a complete theoretical description lies outside the scope of this work, we will now discuss how a non-uniform strain profile is a viable candidate for this rise in HH-LH mixing as V_B is varied. Strain originates from the differences in thermal contraction between the gate electrodes defining the quantum dots and the substrate. This strain can both alter Δ_{HL} and directly mix the HH and LH states, where these effects are greatest along the edges of the confinement gates [20–22]. In one case, Corley-Wiciak et al., 2023 measured the strain profile of a gate-defined quantum dot device and simulated that Δ_{HL} can vary as much as 4% [22]. Although this percentage seems small at first glance, the degree of mixing between the HH and LH states scales as $\left(\frac{1}{\Delta_{HL}}\right)^2$ [23], where even admixtures of 1% significantly reduce g_\perp [16].

From a rough calculation of the quantum dot positions as a function of V_B (see section SVI) and using the results of Ref. [22] for a qualitative picture, we estimate an overall shift of the right dot's position away from the middle barrier leads to a $\sim 3\%$ decrease in Δ_{HL} as the dot moves into a region of increased strain (see Fig. 5c). With this change leading to a 9% enhancement in the LH admixture, we can expect a decrease in both \bar{g} and Δ_{ST_-} . We want to stress these values are crude calculations and only serve as a guide to how the hole g -tensor evolves with respect to V_B and explain the trends in Fig. 5.

IV. CONCLUSION

In summary, we have explored the coherent oscillations in a Ge hole double dot between the singlet, $|S\rangle$, and polarized triplet state, $|T_- \rangle$. The dephasing time of this manipulation strongly depends on the operation detuning with a maximum of $T_2^* = 600$ ns, while the spin relaxation time at the readout point was measured to be $T_1 = 17.2 \mu\text{s}$. The maximum in T_2^* coincides with the minimum in the $S - T_-$ energy splitting, where the system is insensitive to the noise disturbing J and \bar{E}_z .

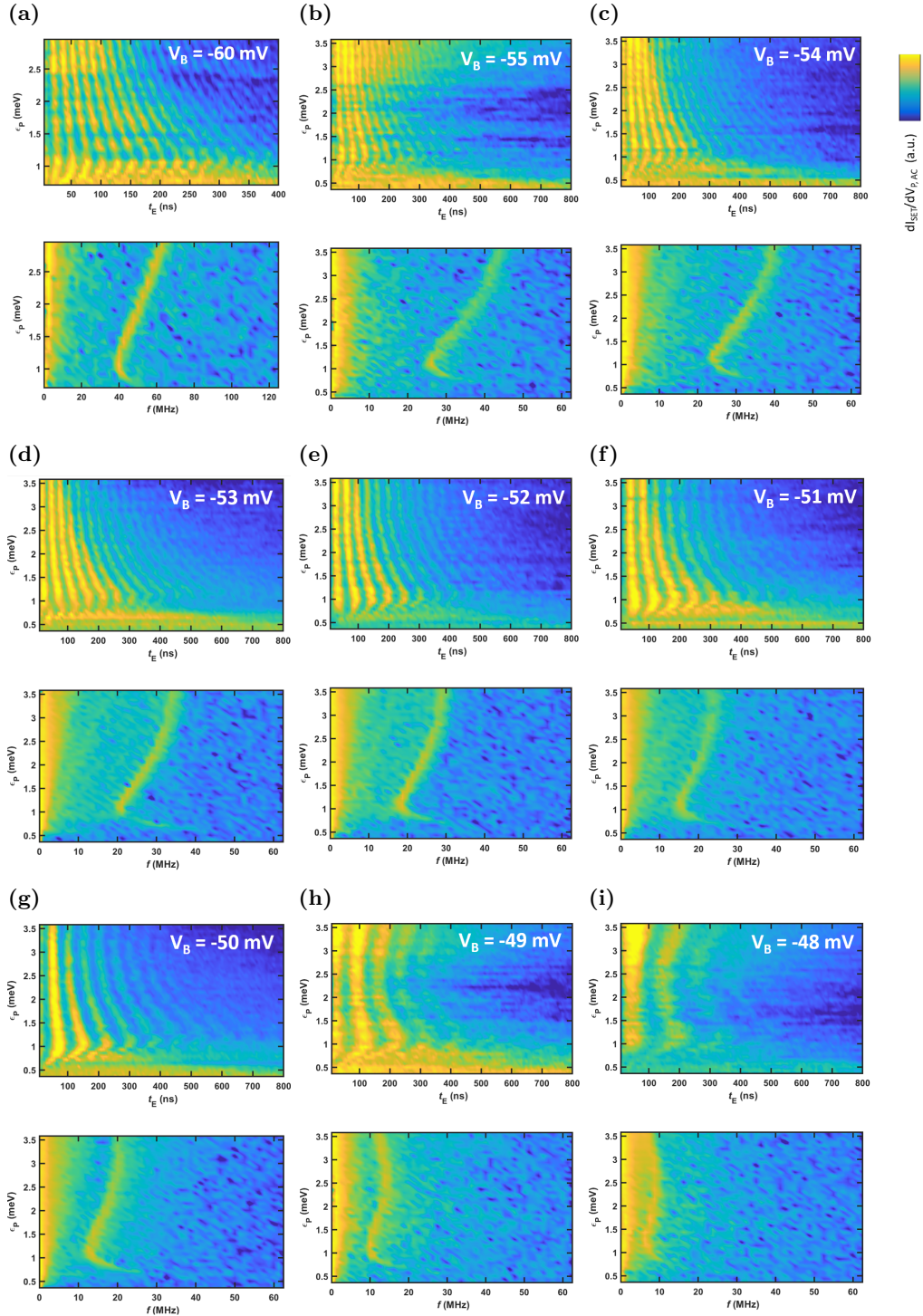


FIG. 4: **(a)-(i)** Evolution of the $S - T_-$ oscillations (upper panel) and their corresponding FFTs (lower panel) as a function of the middle barrier gate voltage V_B . Applying a more positive barrier gate voltage decreases the frequency of the oscillations throughout the entire detuning range. Both the minimum and maximum frequencies decrease as V_B becomes more positive, indicating a reduction in both Δ_{ST_-} and \bar{g} .

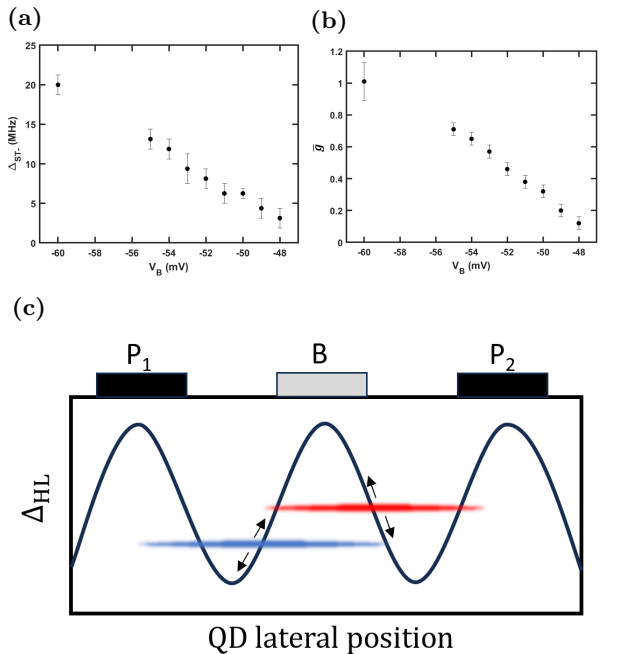


FIG. 5: **(a)** Δ_{ST} as a function of barrier voltage. Values are extracted from the minimum frequency of the FFTs shown in Fig. 4. **(b)** \bar{g} is extracted from frequency at large detunings in Fig. 4 and plotted versus the barrier voltage. Both parameters show a strong linear dependence on the barrier gate voltage. This behavior can be explained by the dots moving through a non-uniform strain environment, which directly impacts the g -factors of each dot. Error bars for (a) and (b) are calculated from the linewidth of the Fourier transform data. **(c)** Cartoon depicting the Δ_{HL} profile underneath the confinement gates due to the effects of strain.

Furthermore, we observe the frequency of evolution between these spin states can be modulated through the voltage of the middle barrier separating the two dots. The frequency dependence on V_B points to the changing dot position over a variable strain profile as the reason for adjusting the qubit frequency. These results suggest strain can be exploited to fine-tune qubit frequencies in Ge. Furthermore, if a variable frequency profile is not desired, the sensitivity of the g -tensor to the quantum dot position can be mitigated by reducing strain in the system, such as by defining gate electrodes with palladium instead of gold to closer match the thermal response of Ge [24].

ACKNOWLEDGEMENTS

Research was sponsored by the Army Research Office (ARO) and was accomplished under Grant No. W911NF-23-1-0016 (at UCLA) and Grant No. W911NF-22-S-0006 (at TU Delft). The views and conclusions contained in this document are those of the authors and should not be interpreted as representing the official policies, either expressed or implied, of the Army Research Office (ARO), or the U.S. Government. The U.S. Government is authorized to reproduce and distribute reprints for Government purposes notwithstanding any copyright notation herein. G.S. also acknowledges support through two “Projectruimte”, associated with the Netherlands Organization of Scientific Research (NWO).

DEVICE FABRICATION

The device was fabricated on top of a Ge/SiGe heterostructure with the strained Ge quantum well buried 55 nm beneath the surface. Ohmic regions were patterned with photolithography and the wafer was dipped in buffered HF (BOE) to remove the thin capping layer of SiO_2 . These regions were then metallized with 60 nm of Pt through e-beam evaporation. We used e-beam lithography to pattern all device leads and a second e-beam evaporation to deposit 5/45 nm of Ti/Au. A 100 nm insulating layer of Al_2O_3 was grown through atomic layer deposition, and a subsequent global top gate was patterned with photolithography. This was followed by a final e-beam evaporation of 100 nm of Al to form the global accumulation gate. The device then underwent a forming gas anneal at 420 C for 1 hour to repair defects in the oxide and anneal the Pt Ohmic regions into the substrate.

MEASUREMENT SETUP

The device was cooled in a Triton dilution refrigerator with a base temperature of 48 mK. All SET current measurements were performed with an SR 830 Lock-in amplifier. When measuring stability diagrams, the lock-in excitation voltage was applied to both plungers and the current through the SET was fed back into the lock-in for integration and demodulation. A voltage pulse to each plunger was supplied by a Tektronix AWG 610 with its pulse frequency modulated by the lock-in. With the lock-in integration time set to 100 ms, 5000 pulse sequences were averaged for each data point during the spin manipulation measurements. All measurements using the AWG pulse were made with no lock-in excitation voltage applied to the plungers. The magnet used was the model B444-N52 produced by K&J Magnetics, Inc. and attached directly next to the device’s PCB. A Hall probe measured the magnetic field at the device’s position on the PCB.

- [1] N. W. Hendrickx, D. P. Franke, A. Sammak, G. Scappucci, and M. Veldhorst, Fast two-qubit logic with holes in germanium, *Nature* **577**, 487 (2020).
- [2] D. Jirovec, A. Hofmann, A. Ballabio, P. M. Mutter, G. Tavani, M. Botifoll, A. Crippa, J. Kukucka, O. Sagi, F. Martins, J. Saez-Mollejo, I. Prieto, M. Borovkov, J. Arbiol, D. Chrastina, G. Isella, and G. Katsaros, A singlet-triplet hole spin qubit in planar ge, *Nature Materials* **20**, 1106 (2021).
- [3] N. W. Hendrickx, W. I. Lawrie, M. Russ, F. van Riggelen, S. L. de Snoo, R. N. Schouten, A. Sammak, G. Scappucci, and M. Veldhorst, A four-qubit germanium quantum processor, *Nature* **591**, 580 (2021).
- [4] G. Scappucci, C. Kloeffel, F. A. Zwanenburg, D. Loss, M. Myronov, J. J. Zhang, S. D. Franceschi, G. Katsaros, and M. Veldhorst, The germanium quantum information route, *Nature Reviews Materials* **6**, 926 (2021).
- [5] M. Lodari, N. W. Hendrickx, W. I. L. Lawrie, T.-K. Hsiao, L. M. K. Vandersypen, A. Sammak, M. Veldhorst, and G. Scappucci, Low percolation density and charge noise with holes in germanium, *Materials for Quantum Technology* **1**, 011002 (2021).
- [6] X. Wu, D. R. Ward, J. R. Prance, D. Kim, J. K. Gamble, R. T. Mohr, Z. Shi, D. E. Savage, M. G. Lagally, M. Friesen, S. N. Coppersmith, and M. A. Eriksson, Two-axis control of a singlet–triplet qubit with an integrated micromagnet, *PNAS* **111**, 11938 (2014).
- [7] J. R. Petta, A. C. Johnson, J. M. Taylor, E. A. Laird, A. Yacoby, M. D. Lukin, C. M. Marcus, M. P. Hanson, and A. C. Gossard, Coherent manipulation of coupled electron spins in semiconductor quantum dots, *Science* **309**, 2180 (2005), <https://www.science.org/doi/pdf/10.1126/science.1116955>.
- [8] B. M. Maune, M. G. Borselli, B. Huang, T. D. Ladd, P. W. Deelman, K. S. Holabird, A. A. Kiselev, I. Alvarado-Rodriguez, R. S. Ross, A. E. Schmitz, M. Sokolich, C. A. Watson, M. F. Gyure, and A. T. Hunter, Coherent singlet-triplet oscillations in a silicon-based double quantum dot, *Nature* **481**, 344 (2012).
- [9] D. Jirovec, P. M. Mutter, A. Hofmann, A. Crippa, M. Rychetsky, D. L. Craig, J. Kukucka, F. Martins, A. Ballabio, N. Ares, D. Chrastina, G. Isella, G. Burkard, and G. Katsaros, Dynamics of hole singlet-triplet qubits with large g -factor differences, *Physical Review Letters* **128**, 10.1103/PhysRevLett.128.126803 (2022).
- [10] C.-A. Wang, G. Scappucci, M. Veldhorst, and M. Russ, Modelling of planar germanium hole qubits in electric and magnetic fields, ” (2022).
- [11] C.-A. Wang, C. Déprez, H. Tidjani, W. I. L. Lawrie, N. W. Hendrickx, A. Sammak, G. Scappucci, and M. Veldhorst, Probing resonating valence bonds on a programmable germanium quantum simulator, *npj Quantum Information* **9**, 1–8 (2023).
- [12] P. M. Mutter and G. Burkard, All-electrical control of hole singlet-triplet spin qubits at low-leakage points, *Physical Review B* **104**, 10.1103/PhysRevB.104.195421 (2021).
- [13] N. W. Hendrickx, L. Massai, M. Mergenthaler, F. Schupp, S. Paredes, S. W. Bedell, G. Salis, and A. Fuhrer, Sweet-spot operation of a germanium hole spin qubit with highly anisotropic noise sensitivity, ” (2023).
- [14] W. I. L. Lawrie, N. W. Hendrickx, F. van Riggelen, M. Russ, L. Petit, A. Sammak, G. Scappucci, and M. Veldhorst, Spin relaxation benchmarks and individual qubit addressability for holes in quantum dots, *Nano Letters* **20**, 7237 (2020), pMID: 32833455, <https://doi.org/10.1021/acs.nanolett.0c02589>.
- [15] I. L. Drichko, V. A. Malysh, I. Y. Smirnov, L. E. Golub, S. A. Tarasenko, A. V. Suslov, O. A. Mironov, M. Kummer, and H. V. Känel, In-plane magnetic field effect on hole cyclotron mass and g_z factor in high-mobility $\text{si}/\text{ge}/\text{si}_{\text{ge}}$ structures, *Physical Review B - Condensed Matter and Materials Physics* **90**, 10.1103/PhysRevB.90.125436 (2014).
- [16] H. Watzinger, C. Kloeffel, L. Vukušić, M. D. Rossell, V. Sessi, J. Kukučka, R. Kirchschrager, E. Lausecker, A. Truhlar, M. Glaser, A. Rastelli, A. Fuhrer, D. Loss, and G. Katsaros, Heavy-hole states in germanium hut wires, *Nano Letters* **16**, 6879 (2016).
- [17] N. Ares, V. N. Golovach, G. Katsaros, M. Stoffel, F. Fournel, L. I. Glazman, O. G. Schmidt, and S. D. Franceschi, Nature of tunable hole g factors in quantum dots, *Physical Review Letters* **110**, 10.1103/PhysRevLett.110.046602 (2013).
- [18] A. A. Kiselev, K. W. Kim, and E. Yablonoitch, In-plane light-hole (formula presented) factor in strained cubic heterostructures, *Physical Review B - Condensed Matter and Materials Physics* **64**, 10.1103/PhysRevB.64.125303 (2001).
- [19] A. V. Nenashev, A. V. Dvurechenskii, and A. F. Zinovieva, Wave functions and g factor of holes in ge/si quantum dots, *Physical Review B - Condensed Matter and Materials Physics* **67**, 10.1103/PhysRevB.67.205301 (2003).
- [20] T. Nakaoka, T. Saito, J. Tatebayashi, and Y. Arakawa, Size, shape, and strain dependence of the g factor in self-assembled $\text{in}(\text{ga})\text{as}$ quantum dots, *Phys. Rev. B* **70**, 235337 (2004).
- [21] S. D. Liles, F. Martins, D. S. Miserev, A. A. Kiselev, I. D. Thorvaldson, M. J. Rendell, I. K. Jin, F. E. Hudson, M. Veldhorst, K. M. Itoh, O. P. Sushkov, T. D. Ladd, A. S. Dzurak, and A. R. Hamilton, Electrical control of the g tensor of the first hole in a silicon mos quantum dot, *Phys. Rev. B* **104**, 235303 (2021).
- [22] C. Corley-Wiciak, C. Richter, M. H. Zoellner, I. Zaitsev, C. L. Manganelli, E. Zatterin, T. U. Schüllli, A. A. Corley-Wiciak, J. Katzer, F. Reichmann, W. M. Klesse, N. W. Hendrickx, A. Sammak, M. Veldhorst, G. Scappucci, M. Virgilio, and G. Capellini, Nanoscale mapping of the 3d strain tensor in a germanium quantum well hosting a functional spin qubit device, *ACS Applied Materials & Interfaces* **15**, 3119 (2023), pMID: 36598897, <https://doi.org/10.1021/acsami.2c17395>.
- [23] J. W. Luo, G. Bester, and A. Zunger, Supercoupling between heavy-hole and light-hole states in nanostructures, *Physical Review B - Condensed Matter and Materials Physics* **92**, 10.1103/PhysRevB.92.165301 (2015).
- [24] B. C. H. Mooy and N. S. Lai, Strain effects in a double dot quantum dot system, in *2022 International Conference on Edge Computing and Applications (ICECAA)* (2022) pp. 1635–1640.

[25] W. G. V. D. Wiel, S. D. Franceschi, J. M. Elzerman, T. Fujisawa, S. Tarucha, and L. P. Kouwenhoven, *Electron transport through double quantum dots* (2002).

Supplementary Materials

I. AWG PULSE SEQUENCE

Fig. S1 outlines the AWG voltage pulse applied to the plungers to manipulate the hole configuration between points R (reset), M (measurement and initialization), and O (operation). To coherently manipulate the two-hole state, we first reset the system at R for $1 \mu\text{s}$, allowing holes to tunnel off both dots until the (0,1) configuration is reached. A hole was then loaded into the right dot by waiting at M for $0.5 \mu\text{s}$ to initialize the system into the singlet ground state $S(0,2)$. The $|S\rangle$ state was generated by quickly pulsing to ϵ_X with a 1 ns rise time. From this ramp and a 10 ns idle period at ϵ_X , a mixture between $|S\rangle$ and $|T_-\rangle$ is created. The system is then moved to the operation point at ϵ_P for an evolution time t_E before the process was reversed to arrive back at M for measurement of the final state.

To read out the final two-hole state, the system was held at point M for $20 \mu\text{s}$. Point M sits inside the Pauli spin blockade (PSB) region, enabling spin to charge conversion when reading out the spin state of the double hole system. Due to spin conservation while in the PSB region, the SET current will either detect a change in the hole configuration to (0,2), signifying the final state as $|S\rangle$, or no change in hole occupation will be seen, indicating the final state as $|T_-\rangle$.

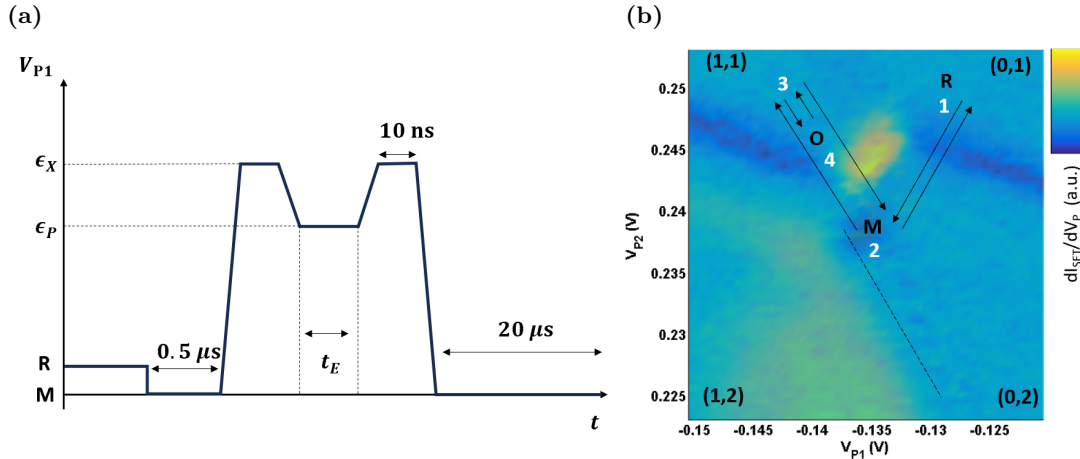


FIG. S1: **(a)** AWG pulse applied to P_1 to observe coherent evolution between the singlet and triplet states (not to scale). The same pulse but inverted (excluding step R) is applied to P_2 . All ramp times were set to 1 ns. **(b)** Two stability diagrams overlaid on top of each other—one scan made with the AWG pulse on and the other scan without the AWG pulse. A dark blue spot appears below the interdot transition line with the pulse on, which we use to mark the measurement position M. Numbers denote the sequence the system undergoes with the AWG pulse. (1) The state is first reset at R for $0.5 \mu\text{s}$, then (2) moved to M for initialization (also $0.5 \mu\text{s}$). (3) The singlet is pulsed deep into (1,1) and allowed to evolve for 10 ns. (4) This ramp is followed by evolution at point O where the system idles at ϵ_P for time t_E . A final rotation is performed at (3) to project the state back onto the singlet and triplet states, where readout is performed at (M) for $20 \mu\text{s}$. Finally, the system is reset at R before undergoing this cycle again.

II. T_2^* DEPHASING

To measure T_2^* , we extracted the decay of oscillations between $|S\rangle$ and $|T_-\rangle$ in Fig. 2a. Each linecut along ϵ_P is fit to the equation $P = Ae^{-(t/T_2^*)^2} \cos(\omega t + B) + Ce^{-t/D} + E$, where A, B, C, D , and E are fitting parameters in addition to T_2^* . The angular frequency $\omega = 2\pi f$ is already known from the Fourier transform data. Several fitted traces are shown in Fig. S2 for Fig. 4f, where the background ($Ce^{-t/D} + E$) has been subtracted off. A clear dependence of the dephasing time on detuning can be seen, where T_2^* continues to decrease past $\epsilon = 1$ meV.

As discussed in the main text, the dependence of T_2^* on ϵ_P can be explained by contributions from electrical and magnetic noise affecting the Zeeman terms in our Hamiltonian (Eqn. 1). For detunings on either side of the $S - T_-$ anticrossing at ϵ_* , $J - \bar{E}_z$ sets the f of evolution. In this region, the noise affecting t_c and \bar{E}_z dominates. We want to note for $\epsilon \ll \epsilon_*$, charge noise disturbing the exchange term J governs T_2^* ; however, that regime was not measured here. For $\epsilon \gg \epsilon_*$, the $S - T_-$ energy levels become increasingly parallel to each other. Once again, \bar{E}_z determines the energy splitting and consequently $\delta\bar{E}_{z_{\text{rms}}}$ is the leading noise source.

Near ϵ_* , the evolution frequency reaches a minimum as the exchange and average Zeeman energy balance each other out, leaving $f = \frac{2\Delta}{h}$ and $\delta\Delta_{\text{rms}}$ setting T_2^* . Because $\delta\Delta_{\text{rms}} < \delta\bar{E}_{z_{\text{rms}}}$, a peak is seen in T_2^* at $\epsilon^* = 1$ meV in Fig. 3a.

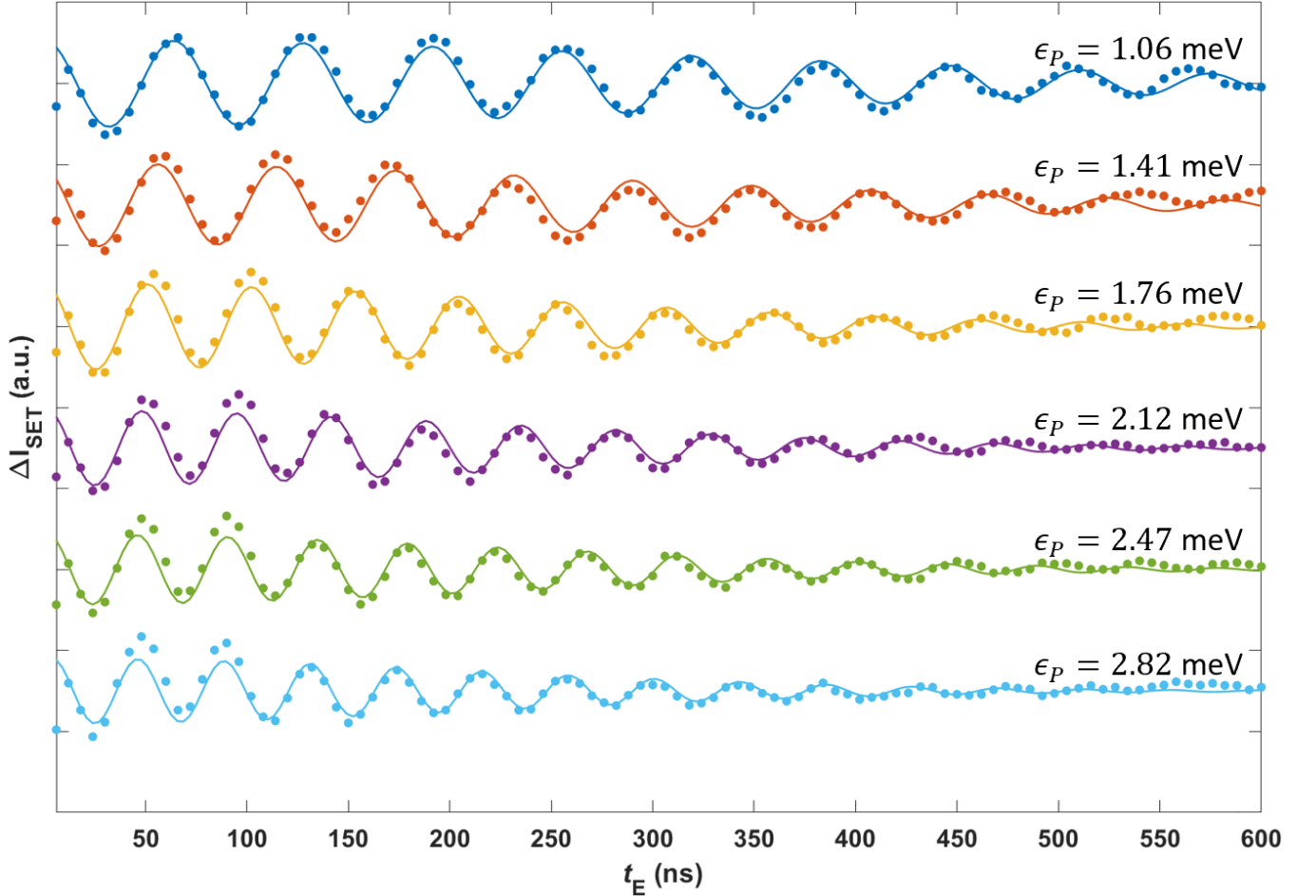


FIG. S2: Traces taken from Fig. 4f for several values of operation detuning ϵ_P . Each trace is fit to a decaying sinusoid with an exponential background and offset. The background is removed before plotting the change in the SET current (ΔI_{SET}) for both the trace and fit (solid line). Each trace is offset along the vertical axis for clarity.

III. LEVER ARM MEASUREMENT

When a small bias voltage V_{SD} is applied across the reservoirs of the double quantum dot, conductance regions in the shape of triangles will form at the intersections of charge transitions between the two dots [25]. The dimensions of these triangles are directly related to the energy separation between the source and drain, eV_{SD} , and the chemical potential of each dot being controlled by its respective plunger voltage:

$$\alpha\Delta V_g = |eV_{SD}|,$$

where α is the lever arm relating the plunger voltage to the dot chemical potential. By measuring the lengths of these triangles along each plunger voltage axis (Fig. S3), we determined the conversion factor α from the ratio of plunger voltage to energy: $\alpha = eV_{SD}/\Delta V_P$. We find the lever arms for P_1 and P_2 to be $\alpha_1 = 0.12$ and $\alpha_2 = 0.11$ eV/V, which were used to convert the plunger voltages to energies for all calculations in this work.

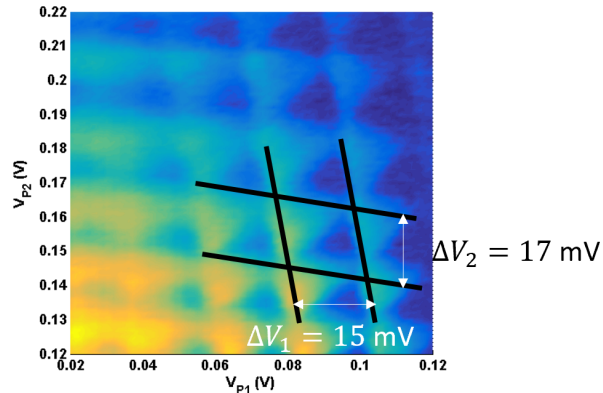


FIG. S3: Stability diagram illustrating transport through both quantum dots with a bias voltage $V_{SD} = 1$ mV across the source-drain reservoirs. Triangles can be seen where the dot charging lines intersect. The dimensions of these triangles are directly related to the source-drain bias and plunger voltage, which we used to calculate the lever arm of each plunger: $\alpha_1 = 0.12$ and $\alpha_2 = 0.11$ eV/V.

IV. FAST $S - T_-$ OSCILLATIONS

The fastest oscillations we observed are shown in Fig. S4. This scan was taken at a center barrier voltage of $V_B = -180$ mV, and illustrates Δ_{ST_-} reaching 75 MHz and the maximum $S - T_-$ energy splitting surpassing 180 MHz, which corresponds to a maximum $\bar{g} \approx 2.8$. While this \bar{g} is larger than those reported in the main text, we do not expect \bar{g} to grow indefinitely as we decrease the middle barrier voltage. As V_B draws the two dots closer to the middle barrier's edge, the continuous increase in tunnel coupling t_c between the two dots will eventually make system inoperable as a singlet-triplet qubit.

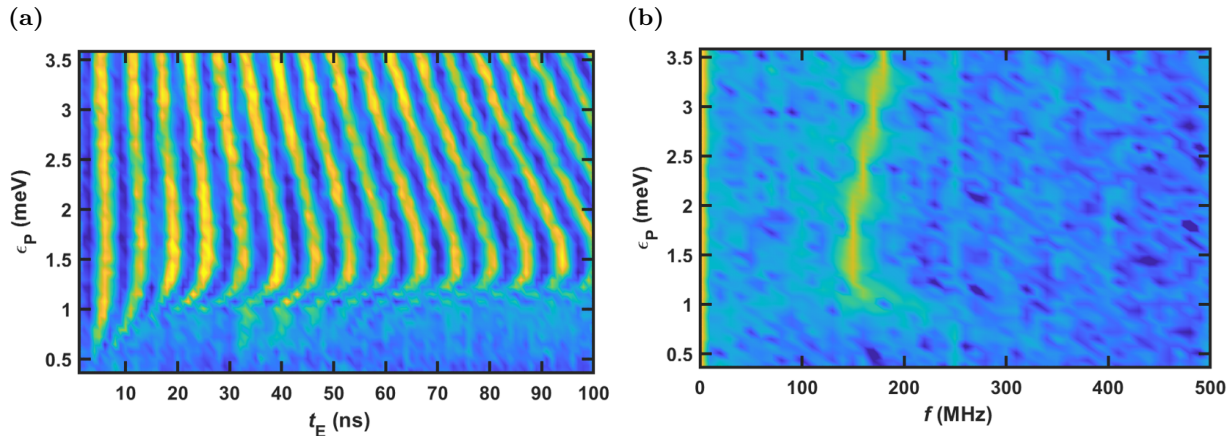


FIG. S4: (a) A scan of the singlet-triplet evolution illustrating the highest frequency oscillations seen from our data set. (b) The the FFT of (a). The $S - T_-$ anticrossing gap is $\Delta_{ST_-} = 75$ MHz, while the frequency at large detunings reaches 180 MHz, signifying $\bar{g} = 2.8$.

V. SINGLET-TRIPLET SPLITTING IN (0,2) FOR READOUT

The energy splitting between the singlet and triplet states in the (0,2) charge configuration was measured by varying the readout position ϵ_r of the Ramsey pulse. As the readout position is further pushed deeper into the (0,2) charge configuration, it will eventually surpass the Pauli spin blockade (PSB) boundary the SET uses to distinguish the singlet and triplet states. While in the PSB region, only the singlet (1,1) state is energetically allowed to tunnel to the singlet (0,2) state. In contrast, all triplet states are prohibited from tunneling to (0,2) due to large singlet-triplet splitting $E_{ST_{02}}$ in the (0,2) charge configuration. The triplet states also are prevented from tunnelling to the singlet (0,2) state due to the conservation of spin.

However, When the readout position is sufficiently pushed deep enough into the (0,2) charge configuration, that is $\epsilon_r > E_{ST_{02}}$, it will be energetically allowed for both the singlet and triplet (1,1) states to tunnel to their respective (0,2) configurations while conserving spin. At this point, the readout position is outside of the PSB region and the SET will no longer distinguish the singlet from the triplet states. From Fig. S5, we measure this cutoff and therefore $E_{ST_{02}}$ to be 0.9 meV.

Knowing the orbital energy difference defines the (0,2) singlet-triplet splitting, we can use $E_{ST_{02}}$ to estimate the size of the right dot by approximating the confinement potential to be a 2d box and the dot shape to be a disk:

$$E_{ST_{02}} = \frac{3\hbar^2\pi^2}{2m^*L^2}$$

$$E_{ST_{02}} = \frac{3\hbar^2\pi^2}{2m^*\pi r^2},$$

where $m^* = 0.09m_e$ and r is the radius of the dot. From $E_{ST_{02}} = 0.9$ meV, we calculate the radius of the right dot to be $r = 66$ nm. By comparing the charging energies of the left and right dot and using the fact that $E \sim 1/r^2$, we further estimate the size of the left dot to be $r = 75$ nm.

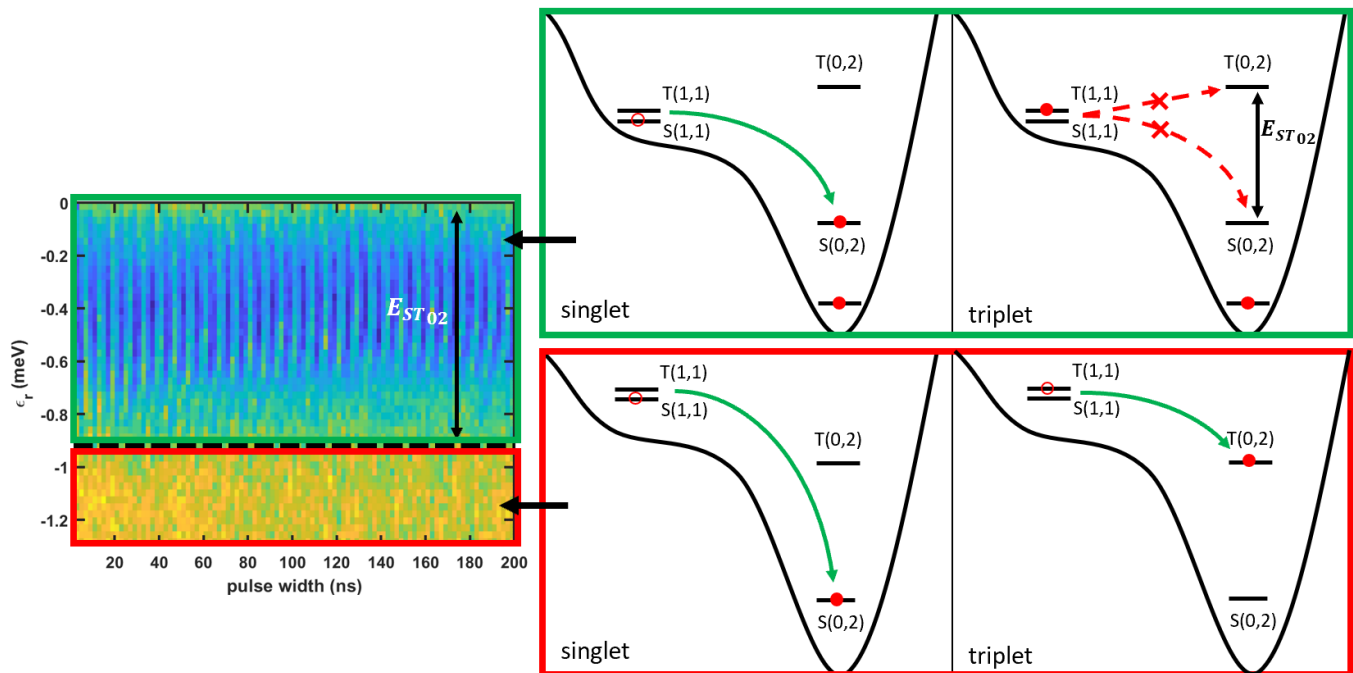


FIG. S5: By scanning the readout position ϵ_r of the Ramsey pulse, we measured the energy splitting between the singlet and triplet states in the (0,2) charge configuration. As the readout position is moved further into (0,2), PSB is eventually lifted as the (1,1) triplet state is allowed to tunnel to the (0,2) triplet. By detecting the readout position where this transition occurs, we measured $E_{ST_{02}} = 0.9$ meV.

VI. ESTIMATION OF Δ_{HL} FROM DOT POSITIONS

We were able to make a crude estimate of the quantum dot positions using capacitance ratios of the quantum dot to the two plungers and barrier gates. The capacitance ratios were found from the slope of the charging lines in the stability diagram. From the relative strength of the effect two gates have on a dot and knowing the gate positions in the x-y plane, we can create what is known as an Apollonian circle. Creating Apollonian circles for two different pairs of gates allowed us to estimate the dot position where these two circles intersect. Repeating this process for various V_B generated the data in Fig. S6.

From Fig. S6, the left dot moves back and forth around its starting position, whereas the right dot generally moves towards the upper right in the x-y plane. From the right dot's relative shift of ~ 36 nm, we estimated the change to Δ_{HL} . Using the simulated data in Ref. [22], we note a maximum change of $\sim 4\%$ in the HH-LH splitting. Compared to the device in this study, the quantum well in Ref. [22] is situated closer to the confinement gates, which greatly increases the effects of strain. Consequently, we only wish to use this 4% change in Δ_{HL} as a guide for understanding the pattern of our data. We expect the modification to Δ_{HL} to be minimized directly underneath an electrode and greatest between two electrodes, which is a distance of 50 nm in our device. Naively assuming a linear dependence of the strain on the dot's position underneath the gates, we can estimate the change in Δ_{HL} from the 36 nm shift in the right dot:

$$\delta\Delta_{HL} \sim \frac{4\%}{50\text{nm}} 36\text{nm} = 3\%.$$

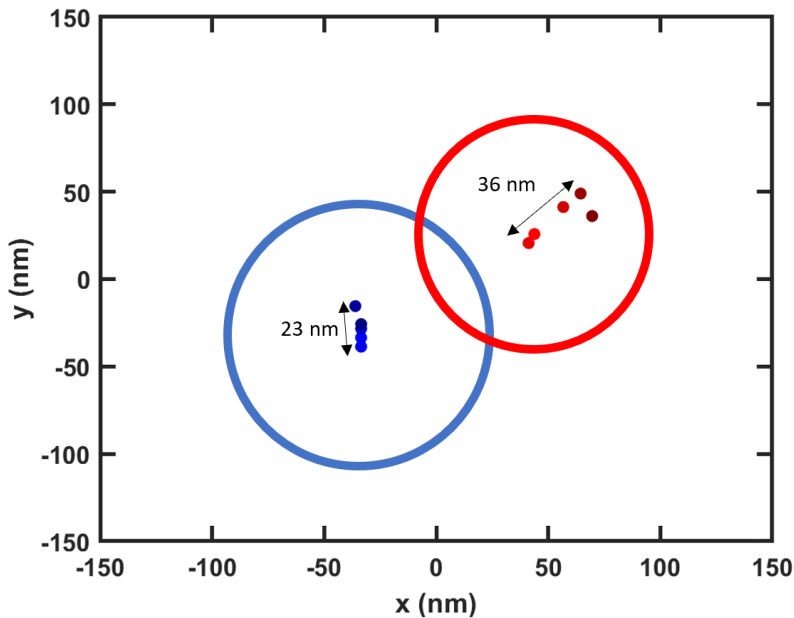


FIG. S6: The positions of both quantum dots are estimated from their capacitance ratios to the two plungers and center barrier. The coordinate $x = 0$ is where the center barrier is placed. Blue (red) dots correspond to the left (right) dot positions. The darker shades correspond to more positive V_B . It is evident that as V_B increases, the right dot tends to shift away from the center barrier, while the left dot fluctuates around its starting position. The diameters of the two quantum dots are depicted as circles and estimated in section SV.